LA-UR-14-24315

| | |
|---|---|
| Title: | Residual Monte Carlo High-Order Solver for Moment-Based Accelerated Thermal Radiative Transfer Equations |
| Author(s): | Willert, Jeffrey A.<br>Park, Hyeongkae |
| Intended for: | The Journal of Computational Physics |
| Issued: | 2014-06-12 |

# Residual Monte Carlo High-Order Solver for Moment-Based Accelerated Thermal Radiative Transfer Equations

Jeffrey Willert[a], H. Park[a]

[a]*Theoretical Division, MS B216, Los Alamos National Laboratory, Los Alamos, NM 87545*

## Abstract

In this article we explore the possibility of replacing standard Monte Carlo (SMC) transport sweeps within a Moment-Based Accelerated Thermal Radiative Transfer (TRT) algorithm with a Residual Monte Carlo (RMC) formulation. Previous Moment-Based Accelerated TRT implementations have encountered trouble when stochastic noise from SMC transport sweeps accumulates over several iterations and pollutes the low-order system. With RMC we hope to significantly lower the build-up of statistical error at a much lower cost. First, we display encouraging results for a zero-dimensional test problem. Then, we demonstrate that we can achieve a lower degree of error in two one-dimensional test problems by employing a RMC transport sweep with multiple orders of magnitude fewer particles per sweep. We find that by reformulating the high-order problem, we can compute more accurate solutions at a fraction of the cost.

*Keywords:* Thermal Radiative Transfer, Moment-Based Acceleration, Monte Carlo, Residual Monte Carlo

## 1. Introduction

Recent work has demonstrated the impressive efficiency with which moment-based acceleration (or High-Order/Low-Order (HO-LO)) techniques can be used to accelerate the solution to the thermal radiative transfer (TRT) equations [1, 2, 3]. Furthermore, recent studies have considered a hybrid method which uses Monte Carlo algorithms to solve the transport equation in the context of moment-based acceleration [1, 4, 5, 6]. These hybrid methods in

which high-order (HO) Monte Carlo solutions are accelerated using a low-order (LO) Moment-Based system have been successful, however not without some struggle. While Monte Carlo methods can provide an exact treatment of complex geometries, are void of discretization error and are highly parallelizable, these solutions can contain a significant amount of statistical error which has the potential to corrupt the LO solver.

We are interested in solving the gray TRT equation

$$\frac{1}{c}\frac{\partial I}{\partial t} + \hat{\Omega} \cdot \nabla I + \sigma I = \frac{\sigma a c T^4}{4\pi}, \tag{1}$$

in which $I = I(\vec{r}, \hat{\Omega}, t)$, the radiation angular intensity, is a function of space, angle and time, $\sigma = \sigma(\vec{r}, T)$, the opacity, is a function of space and temperature, and $T = T(\vec{r}, t)$, the temperature, is a function of space and time. Additionally, $a$ is the radiation constant and $c$ is the speed of light. Equation 1 is coupled to the nonlinear temperature ODE,

$$\rho c_v \frac{\partial T}{\partial t} - \int_{4\pi} d\hat{\Omega} \left( \sigma I - \frac{\sigma a c T^4}{4\pi} \right) = 0, \tag{2}$$

in which $\rho$ and $c_v$ are the density and specific heat of the material, respectively. We refer to the combination of Equations 1 and 2 as the HO system. We apply a backward-Euler time-discretization to the HO system,

$$\frac{I^{n+1} - I^n}{c\Delta t} + \hat{\Omega} \cdot \nabla I^{n+1} + \sigma^{n+1} I^{n+1} = \frac{\sigma^{n+1} a c (T^{n+1})^4}{4\pi}, \tag{3}$$

$$\rho c_v \frac{T^{n+1} - T^n}{\Delta t} - \int_{4\pi} \sigma^{n+1} \left( I^{n+1} - \frac{a c (T^{n+1})^4}{4\pi} \right) d\hat{\Omega} = 0. \tag{4}$$

This system can be solved using source iteration [1, 2] in which $I^{n+1}$ and $T^{n+1}$ are iterated in Equations 3 and 4 until a consistent solution is found. This iteration may converge exceptionally slowly and makes source iteration an impractical choice of solvers when there exists strong absorption-emission physics. Instead, we opt for a moment-based acceleration technique. First we define $E$ and $\vec{F}$, the radiation energy density and radiative flux, respectively, as the $0^{th}$ and $1^{st}$ angular moments of the radiation angular intensity,

$$E = \frac{1}{c} \int_{4\pi} d\hat{\Omega} I \tag{5}$$

$$\vec{F} = \int_{4\pi} d\hat{\Omega} \hat{\Omega} I. \tag{6}$$

2

Now, we define the $0^{th}$ and $1^{st}$ angular moments of Equation 1,

$$\frac{\partial E}{\partial t} + \nabla \cdot \vec{F} + c\sigma E = \sigma a c T^4, \tag{7}$$

$$\frac{1}{c}\frac{\partial \vec{F}}{\partial t} + \nabla \cdot \mathcal{E}cE + \sigma \vec{F} = 0, \tag{8}$$

in which we define the Eddington tensor, $\mathcal{E}$,

$$\mathcal{E} = \frac{\int_{4\pi} d\hat{\Omega}\hat{\Omega}\hat{\Omega}I}{\int_{4\pi} d\hat{\Omega}I}. \tag{9}$$

We refer to Equations 7 and 8 as the LO system.

As in [7], we replace $\mathcal{E}$ with the $P_1$ approximation and a consistency term, $\gamma$, to enforce HO-LO consistency,

$$\frac{1}{c}\frac{\partial \vec{F}}{\partial t} + \frac{c}{3}\nabla E + \sigma \vec{F} = \gamma c E. \tag{10}$$

Lastly, we can rewrite the temperature equation in terms of $E$,

$$\rho c_v \frac{\partial T}{\partial t} - \left(\sigma c E - \sigma a c T^4\right) = 0. \tag{11}$$

The LO system, Equations 7, 10, and 11, can be solved efficiently using modern nonlinear solvers [12, 13]. The solution of the LO system provides an explicit expression for the emission source in Equation 3 and thus there is no need for iteration within the HO system. As a result, this HO-LO method accelerates the solution to the original TRT system.

Now, we can define a predictor-corrector algorithm [2] which allows us to solve the TRT system at each time-step, Algorithm 1.

Using Algorithm 1, we only need to execute a single HO solve at each time-step. A *HO solve* is defined to be the operation applied by inverting the left-hand-side operator of Equation 3 (transport operator). This operation is generally considered to be a major computational cost. This HO-LO algorithm allows a single HO solve per time-step by using the LO system to provide a consistent $T^4$ (emission) source. This is a major advantage over source iteration, in which the number of HO solves per time-step can be excessive, and is a more accurate option than those algorithms which utilize a linearization of the source term. HO solves are often referred to as *transport sweeps* when the high-order solver is deterministic in nature. We adopt

3

this convention when stochastic solvers are used as well, referring to them as *Monte Carlo transport sweeps*.

The authors of [1] demonstrated that Equation 12 can be solved using a Monte Carlo (MC) transport sweep so long as an adequate number of particles is used. We assume that the HO transport sweep "inverts" the transport operator accurately, however this is not necessarily the case when an MC HO solver is used. Within the HO-LO context, the MC solver must obtain an accurate global solution which is generally inefficient. When too few particles are used, undersampling and statistical noise can corrupt the consistency term, $\gamma^{n+1}$, so much that the LO solver may fail to converge. Unfortunately, in these calculations we do not always have the luxury of increasing the particle count per transport sweep to a level which will achieve a suitably-low level of noise.

Instead of attempting to increase the number of particles per sweep or replacing the noisy solution with an asymptotic approximation in some regions of the domain [1], we seek to replace the standard Monte Carlo (SMC) solver with a highly accurate Residual Monte Carlo (RMC) approach.

## 2. Residual Monte Carlo

For one reason or another, we often know the exact solution in some region of the domain or can approximate the solution using a diffusion model or the previous time-step. In this case, asking an SMC simulation to resolve $I^{n+1}$ is an inefficient use of computational resources. Suppose we have a good approximation, $I^+$, to $I^{n+1}$, in which

$$|\delta^{n+1}| = |I^{n+1} - I^+| \ll |I^{n+1}|. \tag{13}$$

In this case, if we write a residual equation for $\delta^{n+1}$,

$$\frac{\delta^{n+1}}{c\Delta t} + \hat{\Omega} \cdot \nabla \delta^{n+1} + \sigma^{n+1}\delta^{n+1} = \frac{\sigma^{n+1}ac(T^{n+1})^4}{4\pi} + \frac{I^n}{c\Delta t} - \cdots$$
$$\left( \frac{I^+}{c\Delta t} + \hat{\Omega} \cdot \nabla I^+ + \sigma^{n+1}I^+ \right), \tag{14}$$

then the source term (right-hand-side of Equation 14), is smaller than the source term of the original formulation (Equation 3). The error in the simulation is directly proportional to the magnitude of the source term, so intuitively the statistical noise incurred in computing $\delta^{n+1}$ is smaller than if we had attempted to compute $I^{n+1}$ directly.

4

This simple idea opens up the possibility of using a much smaller number of particles for each HO solve in order to achieve more accurate solutions. Furthermore, RMC allows one to distribute MC particles more efficiently within the HO-LO context. However, implementation of the RMC HO solve can be a non-trivial endeavor. Adapting existing SMC codes may be difficult for several reasons. First of all, the code must be willing to accept a negative source when the residual source term loses positivity. Furthermore, as we will demonstrate in later sections, it will be required to build source terms at interior cell-faces. However, as we will see, these adaptations may be well worth the extra effort.

The rest of the paper will follow the same order in which we developed the one-dimensional gray RMC HO solver. We begin by considering an isotropic 0-D problem which is started out of equilibrium and relaxes to an equilibrium solution. At each time-step we can compute an exact solution to Equation 3 for comparison purposes. Then we consider a 0-D problem with an initially anisotropic angular intensity and watch it relax to an isotropic equilibrium. Finally, we walk through the process which led us to the final one-dimensional gray RMC HO solver.

This work is definitely not the first to consider using RMC to solve kinetic systems, however our HO-LO algorithm allows for a much easier implementation in which the Monte Carlo algorithm solves a purely absorbing problem - the re-emission term is handled completely by the LO system. Furthermore, our algorithm requires only a single HO solve per time-step. In [10], the authors demonstrate the use of an exponentially-convergent Monte Carlo algorithm for solving the neutron transport equation which takes advantage of the residual formulation. Their work hinges on the ability to refine the spatial and/or angular mesh throughout the iteration, which they refer to as "mesh adaptation." For our problem, however, mesh adaptation is not a feasible option.

The authors of [8] and [9] solve the TRT equations using a RMC formulation, though in a different form. In these papers the authors define their difference formulation by suggesting that

$$I^{n+1}(x,\mu) \approx \frac{ac(T^{n+1}(x))^4}{2}$$

and define

$$\delta^{n+1}(x,\mu) = I^{n+1}(x,\mu) - \frac{ac(T^{n+1}(x))^4}{2}.$$

Furthermore, the authors demonstrate that when using a piecewise constant approximation of the radiation angular intensity, their mesh must be refined so that each cell is on the order of a single mean-free-path [9]. In Section 4 we demonstrate that we can choose a better approximation to the new time intensity and we show that our piecewise constant approximation can yield the same results as an SMC simulation using vastly fewer particles.

## 3. 0-D Test Problem

We will look at two 0-D test problems. For the first problem we will assume an isotropic angular intensity throughout the simulation. In the second problem, we'll consider an anisotropic initial condition. In this section we will solve the 0-D high-order system, given by

$$\frac{I^{n+1} - I^n}{c\Delta t} + \sigma I^{n+1} = \sigma ac(T^{n+1})^4 \quad (15)$$

$$\rho c_v \frac{T^{n+1} - T^n}{c\Delta t} - \int_{-1}^{1} \left( \sigma I^{n+1} - \sigma ac(T^{n+1})^4 \right) d\mu = 0. \quad (16)$$

For all 0-D test problems we utilize standard track-length tallies whenever a MC simulation is applied as the HO solver. In Section 4.4 we will discuss a better method of tallying, however their use in 0-D would hide the effects of the RMC simulation.

### 3.1. Isotropic Angular Intensity

For this problem, we will demonstrate the effectiveness of RMC using the source iteration algorithm,

$$\frac{I^{n+1,k+1} - I^n}{c\Delta t} + \sigma I^{n+1,k+1} = \sigma ac(T^{n+1,k})^4 \quad (17)$$

$$\rho c_v \frac{T^{n+1,k+1} - T^n}{c\Delta t} - \left( \sigma I^{n+1,k+1} - \sigma ac(T^{n+1,k+1})^4 \right) = 0. \quad (18)$$

We iterate until $\|T^{n+1,k+1} - T^{n+1,k}\| < 10^{-12}$ at each time-step. We avoid use of the HO-LO algorithm in this test problem, as the LO system would give the isotropic angular intensity exactly. The SMC simulation will solve

$$\frac{I^{n+1,k+1}}{c\Delta t} + \sigma I^{n+1,k+1} = \sigma ac(T^{n+1,k})^4 + \frac{I^n}{c\Delta t}. \quad (19)$$

For RMC we will make the approximation that $I^{n+1,k} = I^n + \delta^{n+1,k}$. In this case, the residual equation becomes

$$\frac{\delta^{n+1,k+1}}{c\Delta t} + \sigma\delta^{n+1,k+1} = \sigma ac(T^{n+1,k})^4 - \sigma I^n. \qquad (20)$$

For both SMC and RMC we will utilize a total of $10^4$ particles per HO solve in our computational tests. These solutions will be compared to a deterministic solution of Equation 19 which is exact in the sense that there is no spatial or angular discretization error. We use an initial angular radiation intensity $I^0 = ac(500^4)$ and an initial temperature $T^0 = 50\ eV$. We choose $c_v = 10^{12}\ erg/eV - g$, a material density $\rho = 0.1\ g/cm^3$, and a constant opacity $\sigma = 1000\ cm^{-1}$. We ran the simulation for 1000 time-steps with $\Delta t = 5 \times 10^{-16}\ s$. The deterministic source iteration algorithm requires roughly 2.68 transport sweeps per timestep. The number of SMC transport sweeps per timestep can vary due to MC noise. Using the more accurate RMC transport sweeps, the number of sweeps per timestep is comparable to the deterministic method.

In Figure 1 we plot the relative error in the angular intensity at each time-step. In Figure 2, we plot the relative error in the temperature at each time-step. Clearly, the equilibrium radiation intensity computed via SMC is about 10% off of the true equilibrium, whereas the error is only about .1% off using RMC. These errors are caused by a buildup of minor errors throughout the simulation. In each case, we see that the relative error of RMC is over two orders of magnitude lower when using RMC. It is clear from these two plots that the RMC sweep can provide a significant reduction in error over MC even for a very simple problem without spatial or angular dependence.

### 3.2. Anisotropic Angular Intensity

In this section we will consider solving the 0-D thermal radiative transfer equations when the angular intensity is initially anisotropically distributed. In this case, we will utilize the $0^{th}$ angular moment of Equation 15 in order to bypass the source iteration and accelerate the computation. Now, at each time-step we solve the following LO system,

$$\frac{E^{n+1} - E^n}{\Delta t} + c\sigma E^{n+1} = \sigma ac(T^{n+1})^4, \qquad (21)$$

$$\rho c_v \frac{T^{n+1} - T^n}{c\Delta t} - \left(\sigma c E^{n+1} - \sigma ac(T^{n+1})^4\right) = 0, \qquad (22)$$
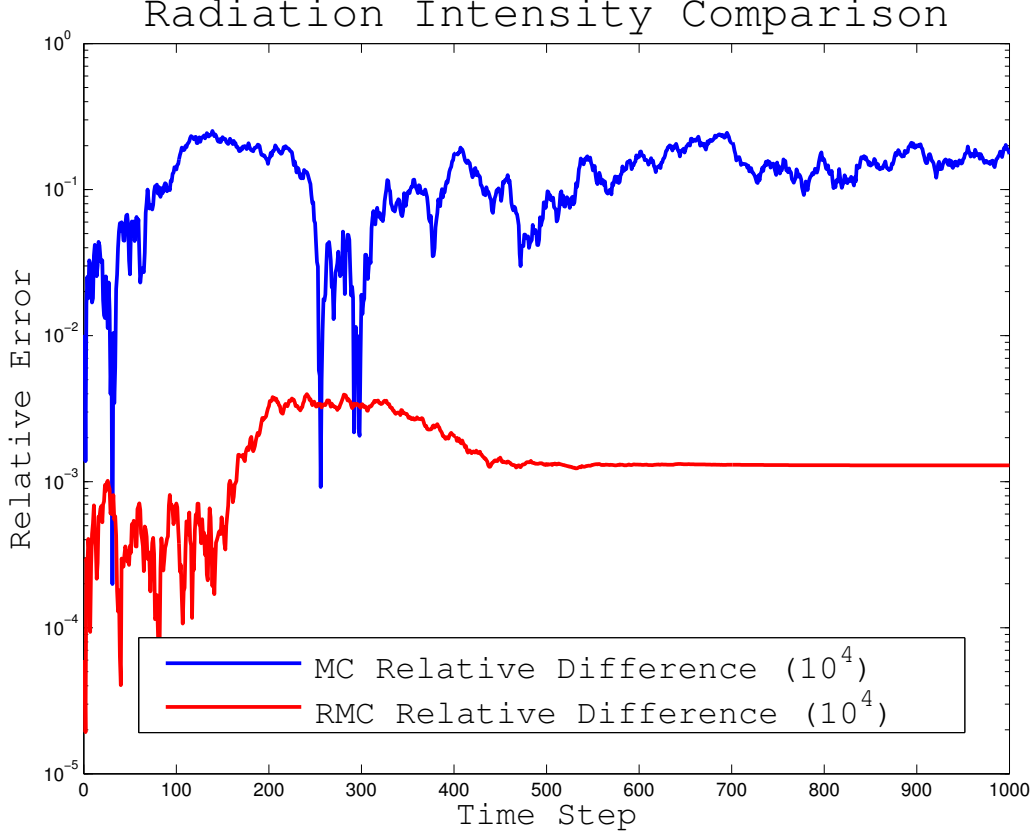
7

Figure 1: Error in the angular intensity at each time-step.

for $E^{n+1}$ and $T^{n+1}$. In this case, $T^{n+1}$ is the correct temperature to use in Equation 15. Therefore, we obtain the correct solution with a single HO solve per time-step. We use the same test problem as before except for the anisotropy of the angular intensity. We use 16 angular bins and the initial intensity is given by

$$I^0(\mu) = \mu^2 ac(500^4). \tag{23}$$

As before, we can compute $\delta^{n+1}$ using

$$\frac{\delta^{n+1}}{c\Delta t} + \sigma\delta^{n+1} = \sigma ac(T^{n+1})^4 - \sigma I^n. \tag{24}$$
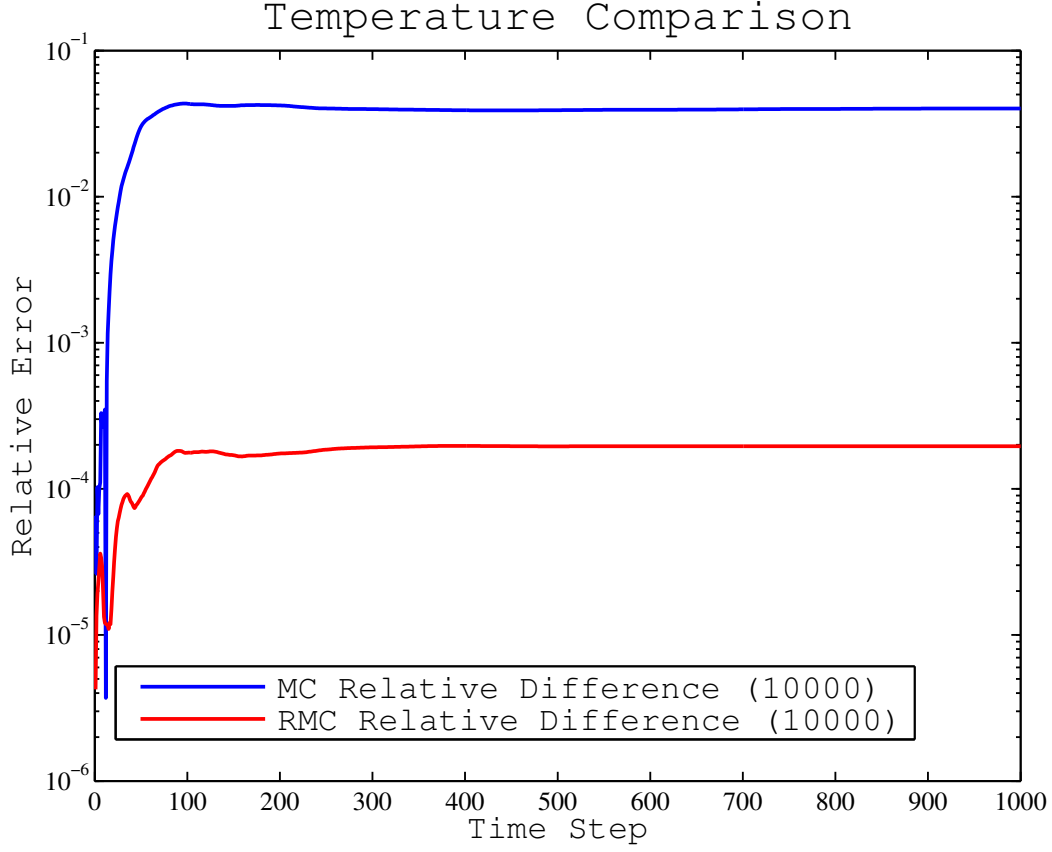
8

Figure 2: Error in the material temperature at each time-step.

However, it should be clear that $\delta^{n+1}$ does contain some amount of stochastic noise and does not satisfy Equation 24 exactly as standard track-length tallies do not conserve energy. In 1-D (and beyond), the use of continuous energy deposition (CED) tallies is warranted [1, 4, 5, 6, 11]. These tallies satisfy that $0^{th}$ moment balance equation and are generally less noisy than the other conservative analog tallies.

## 4. 1-D Residual Monte Carlo

In this section we solve the 1-D TRT system

$$\frac{I^{n+1} - I^n}{c\Delta t} + \mu\frac{\partial I^{n+1}}{\partial x} + \sigma I^{n+1} = \sigma\frac{ac(T^{n+1})^4}{2} \quad (25)$$
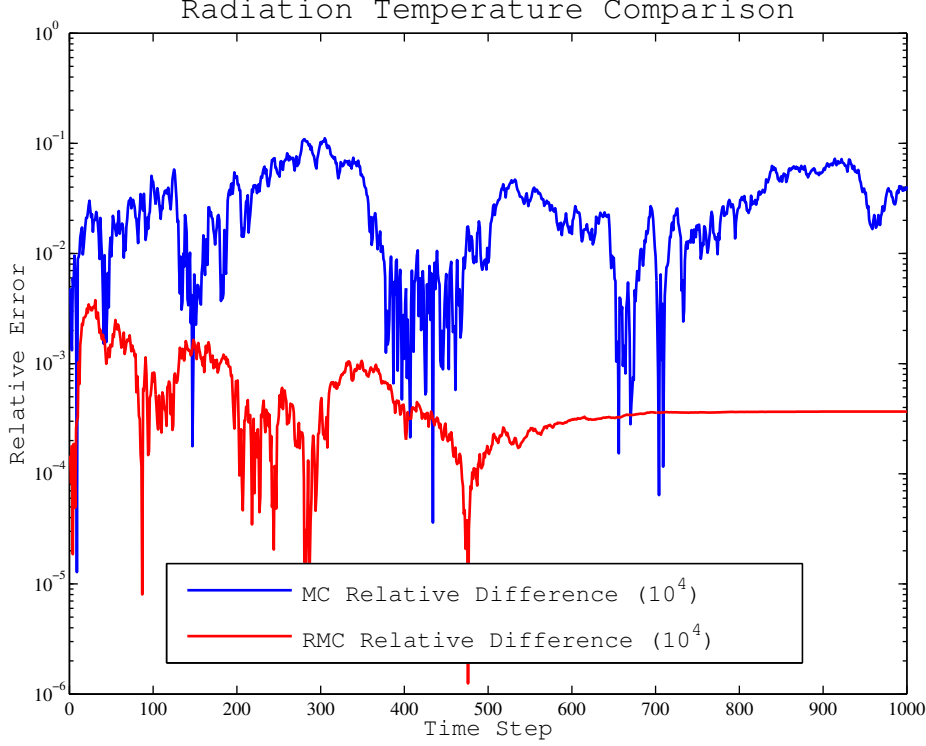
9

Figure 3: Error in the radiation temperature at each time-step.

$$\rho c_v \frac{T^{n+1} - T^n}{c\Delta t} - \int_{-1}^{1} \left( \sigma I^{n+1} - \sigma \frac{ac(T^{n+1})^4}{2} \right) d\mu = 0. \qquad (26)$$

Now we will use Algorithm 1 to advance the simulation in time. In the previous section we were able to easily implement the RMC method and achieve a consistent and correct solution. In 1-D, however, much more care must be taken when deriving the RMC algorithm.

Consider a similar approach to the 0-D case and let $I^{n+1} = I^+ + \delta^{n+1}$, which yields

$$\frac{\delta^{n+1}}{c\Delta t} + \mu \frac{\partial \delta^{n+1}}{\partial x} + \sigma \delta^{n+1} = \sigma \frac{ac(T^{n+1})^4}{2} - \frac{I^+ - I^n}{c\Delta t} - \mu \frac{\partial I^+}{\partial x} - \sigma I^+ . (27)$$

In the continuum, Equation 27 is correct and will produce the correct residual solution. However, once the equation has been spatially discretized, we
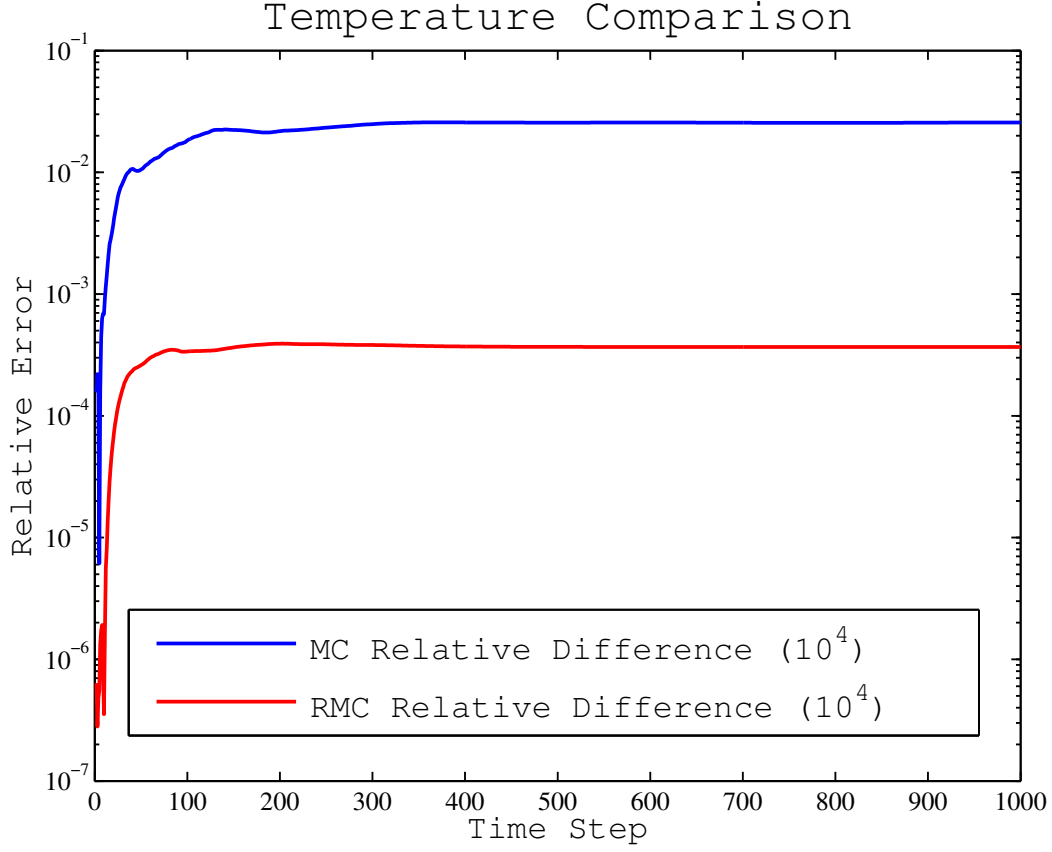
Figure 4: Error in the material temperature at each time-step.

must be careful with the treatment of the $\mu \frac{\partial I^n}{\partial x}$ term on the right-hand-side. When we represent the radiation angular intensity using a constant source in each space-angle cell, we find that both the angular intensity and its spatial derivative are discontinuous. In the remainder of this section we will demonstrate how to evaluate the residual term for an appropriate choice of $I^+$.

### 4.1. Discrete Residual Formulation

In this section we consider a residual formulation where $\delta^{n+1}$ $= I^{n+1} - I^+$, in which $I^+$ is any approximation to $I^{n+1}$. Again, our residual

equation is now given by

$$\frac{\delta^{n+1}}{c\Delta t} + \mu\frac{\partial\delta^{n+1}}{\partial x} + \sigma^{n+1}\delta^{n+1} = \frac{\sigma^{n+1}ac}{2}(T^{n+1})^4 - \frac{I^+ - I^n}{c\Delta t}\cdots$$

$$- \mu\frac{\partial I^+}{\partial x} - \sigma^{n+1}I^+. \tag{28}$$

This formulation allows us to consider volumetric sources and boundary sources separately. We can define two source functions

$$V = \frac{\sigma^{n+1}ac}{2}(T^{n+1})^4 - \frac{I^+ - I^n}{c\Delta t} - \sigma^{n+1}I^+, \tag{29}$$

$$B = -\mu\frac{\partial I^+}{\partial x}, \tag{30}$$

and treat them independently.

The volumetric source, $V$, is treated in the standard way. The boundary source, $B$, yields a delta-function source at each interior and exterior cell boundary. The strength of the face source is based upon the difference in intensities in the two adjacent cells. At a cell face $x_{i+\frac{1}{2}}$, the source is given by

$$B_{i+\frac{1}{2}} = sign(\mu)\left|I_{i+1}^+ - I_i^+\right|. \tag{31}$$

*4.2. Justification for Discrete Residual Formulation*

Consider the solution of the transport equation for a single time-step, in a single cell in which the old-time solution, $I^0(\mu)$, is constant in space. Without loss of generality, assume $\mu > 0$ and choose the left cell boundaries $x_L = 0$. Furthermore, define an incoming source at the left boundary, $I_L = C$, and a new-time temperature, $T^1$, which is also constant throughout the cell.

Then the new time solution of Equation 3 is given by

$$I^1(x,\mu) = Ce^{-\frac{\tilde{\sigma}^1 x}{\mu}} + \left(\frac{\sigma^1 ac(T^1)^4}{2} + \frac{I^0(\mu)}{c\Delta t}\right)\frac{(1 - e^{-\frac{\tilde{\sigma}^1 x}{\mu}})}{\tilde{\sigma}^1}, \tag{32}$$

in which

$$\tilde{\sigma}^1 = \sigma^1 + \frac{1}{c\Delta t}.$$

Now, consider the solution of

$$\frac{\delta_v^1}{c\Delta t} + \mu\frac{\partial\delta_v^1}{\partial x} + \sigma^1\delta_v^1 = \frac{\sigma^1 ac(T^1)^4}{2} - \sigma^1 I^0(\mu). \tag{33}$$

12

with zero boundary conditions. We find

$$
\begin{aligned}
\delta_v^1(x,\mu) &= \left( \frac{\sigma^1 ac(T^1)^4}{2} - \sigma^1 I^0(\mu) \right) \frac{(1 - e^{-\frac{\tilde{\sigma}^1 x}{\mu}})}{\tilde{\sigma}^1} \\
&= \left( \frac{\sigma^1 ac(T^1)^4}{2} - \sigma^1 I^0(\mu) - \frac{1}{c\Delta t} I^0(\mu) + \frac{1}{c\Delta t} I^0(\mu) \right) \frac{(1 - e^{-\frac{\tilde{\sigma}^1 x}{\mu}})}{\tilde{\sigma}^1} \\
&= \left( \frac{\sigma^1 ac(T^1)^4}{2} - \tilde{\sigma}^1 I^0(\mu) + \frac{1}{c\Delta t} I^0(\mu) \right) \frac{(1 - e^{-\frac{\tilde{\sigma}^1 x}{\mu}})}{\tilde{\sigma}^1} \\
&= \left( \frac{\sigma^1 ac(T^1)^4}{2} + \frac{1}{c\Delta t} I^0(\mu) \right) \frac{(1 - e^{-\frac{\tilde{\sigma}^1 x}{\mu}})}{\tilde{\sigma}^1} - I^0(\mu) + I^0(\mu) e^{-\frac{\tilde{\sigma}^1 x}{\mu}}.
\end{aligned}
$$

Furthermore, let us solve

$$
\frac{\delta_b^1}{c\Delta t} + \mu \frac{\partial \delta_b^1}{\partial x} + \sigma^1 \delta_b^1 = 0 \tag{34}
$$

in which $\delta_b^1(0,\mu) = C - I^0(\mu)$. Here, we find,

$$
\delta_b^1(x,\mu) = \left( C - I^0(\mu) \right) e^{-\frac{\tilde{\sigma}^1 x}{\mu}} \tag{35}
$$

and therefore,

$$
I^0 + \delta_v^1 + \delta_b^1 = Ce^{-\frac{\tilde{\sigma}^1 x}{\mu}} + \left( \frac{\sigma^1 ac(T^1)^4}{2} + \frac{1}{c\Delta t} I^0(\mu) \right) \frac{(1 - e^{-\frac{\tilde{\sigma}^1 x}{\mu}})}{\tilde{\sigma}^1}. \tag{36}
$$

So the residual formulation recovers the analytic solution when incorporating cell-surface delta-function sources.

## 4.3. Choosing $I^+$

As one may surmise, the choice of $I^+$ is very important when trying to develop an efficient residual Monte Carlo algorithm. Equation 28 is correct for any choice of $I^+$, however the goal is to minimize the strength of the source, or analogously, minimize the difference between $I^{n+1}$ and $I^+$. It is tempting to use the old time intensity, $I^n$, as an approximation to $I^{n+1}$. In many instances we found that this yielded positive cell face sources and negative cell volumetric sources. While mathematically correct, we found that Monte Carlo integration of these sources was very challenging when $\sigma$ was

13

large. Furthermore, we found that both the volumetric and the face sources could be quite large in magnitude when the solution is sharply varying.

These facts lead us towards a new approach. In order to avoid needing to cancel positive and negative weights within each cell, we found that we could zero out the volumetric source via the appropriate choice of $I^+$. That is, we solve $V = 0$,

$$\frac{\sigma^{n+1}ac}{2}(T^{n+1})^4 - \frac{I^+ - I^n}{c\Delta t} - \sigma^{n+1}I^+ = 0 \tag{37}$$

$$\frac{\sigma^{n+1}ac}{2}(T^{n+1})^4 + \frac{I^n}{c\Delta t} = \frac{I^+}{c\Delta t} + \sigma^{n+1}I^+ \tag{38}$$

$$\left(\frac{1}{c\Delta t} + \sigma^{n+1}\right)^{-1}\left(\frac{\sigma^{n+1}ac}{2}(T^{n+1})^4 + \frac{I^n}{c\Delta t}\right) = I^+ \tag{39}$$

Given this choice of $I^+$, no volumetric sources are required. The corrections to $I^+$ are taken care of entirely by the face sources. The benefit of this increases as the Monte Carlo simulation of face sources is generally more accurate - the stochastic variability of initial particle locations only exists for volumetric sources.

### 4.4. Implementation

Our residual Monte Carlo simulation behaves almost identically to a traditional standard Monte Carlo implementation, however has an additional function which computes the approximation $I^+$. As one can see from Equation 39, the computation of $I^+$ is inexpensive and can be done in parallel – $I^+$ in each space-angle cell is completely independent of each neighboring space-angle cell. Once $I^+$ has been computed, the simulation is ready to begin and particles are instantiated at each cell face with nonzero residual.

One easily overlooked feature of this algorithm is that *there is no error in some regions of the solution in which the spatial gradient is zero using RMC.* This can be seen in Figures 5 - 14. In each of these figures, the RMC solution past the radiation front remains perfectly in equilibrium.

This previous point also illuminates another way in which RMC can be dramatically more efficient than SMC. With SMC, we need to supply enough particles to each cell of the domain so that the radiation angular intensity and cell-face radiative fluxes can be computed accurately. This is not the case with RMC, however. With RMC, we can query the residual before we begin a sweep and place particles based upon the relative strength of the residual.

When the residual is zero in a given region, we need not birth any particles in that portion of the domain. For example, when a domain begins initially in equilibrium and a boundary source is supplied at $t = 0$, we can concentrate nearly all of the particles to the boundary source and the volumetric source in the first few cells as the simulation begins to evolve. This can easily be handled on the fly by pre-computing the residual before each sweep.

In addition, it is important to reiterate that we use continuous energy deposition (CED) tallies [1, 4, 5, 6, 11]. The use of these CED tallies is critical in the implementation of hybrid HO-LO methods. One known deficiency of the combination of track-length tallies and surface crossing tallies is that they do not satisfy the balance equation, Equation 7, for a finite number of particles. CED and surface crossing tallies, however, satisfy the balance equation to round-off error for any number of particles per simulation. The HO-LO method is derived from the consistency of the discrete balance equation. Thus, the CED tallies are a natural choice.

## 5. 1-D RMC Results

In order to objectively analyze and compare the RMC algorithm, we will define a *Figure of Merit* (FoM) which acts as a measure of the efficiency of each algorithm:

$$\text{FoM} = \frac{1}{\|Error\|_2 \times (\text{PPTS})} \tag{40}$$

in which PPTS refers to the average number of particles per transport sweep. This FoM leads to a sensible measure of efficiency – if the error decreases by some factor for the same number of particles, the FoM increases by that factor.

When we refer to the "error", we refer to the absolute error computed in the radiation temperature. When errors are plotted in Figures 5 to 14, the reader should be conscious that the scales on the $y$-axis area *always* different for SMC and RMC. In many cases, the scales on the $y$-axis differ by several orders of magnitude. While this makes head to head comparisons slightly more difficult, it allows the reader to consider the spatial structure of the errors for both SMC and RMC.

In our implementation of the RMC algorithm, each cell face with nonzero residual is guaranteed to have at least one particle born on that face. Particles are distributed based upon the relative strength of the residual source term

on a given face. For this reason, when we request a given number of particles per transport sweep, this number is used as a minimum number of particles to distribute. In many cases, we see that the actual number of particles are a factor of 1 to 4 times more than the requested number of particles. Note that the FoM is evaluated with the actual number of Monte Carlo particles used.

*5.1. 1-D Gray Marshak Wave Test Results*

This problem consists of a single material throughout a 2.0 cm domain. The temperature and intensity are initially in equilibrium at 0.025 eV. At $t = 0$ a 150 eV isotropic source is applied to the left boundary. The opacity for this problem is temperature dependent and given by

$$\sigma(T) = \frac{10^6 \rho}{T^3}.$$

For this problem, $\rho = 1.0 \ g/cm^3$ and $c_v = 1.3784 \times 10^{11} \ erg/eV - g$. We ran each simulation to a final time $t = 5 \times 10^{-8}$ s.

We are interested in observing the sensitivity of the RMC algorithm to the number of particles per transport sweep, time step size, number of spatial cells and number of angular bins. For this reason, we will perform a study in which the timestep size is varied between $10^{-12}$ s to $10^{-10}$ s, while holding the number of cells and angular bins constant. We'll perform a similar study in which the number of angular bins is varied between 16 and 128 and a third study in which we consider two different spatial meshes.

*5.1.1. Sensitivity to Timestep Size*

In this section we will solve the Marshak wave problem using timestep sizes $\Delta t = 10^{-12}$ s, $10^{-11}$ s and $10^{-10}$ s. We fix the number of spatial cells equal to 20 and use 64 angular bins. The error is computed using a high-accuracy step-characteristics solution on the same spatial-mesh using the same time-step size. We compute the FoM for both SMC and RMC where the FoMs have been normalized so that the FoM for SMC using 500 particles is 1. The FoMs are displayed in Table 1.

In Figures 5 and 6 we plot the error for SMC and RMC at timestep sizes of $10^{-12}$ s and $10^{-10}$ s. At $\Delta t = 10^{-12}$ s, RMC is far more efficient than SMC. From Figure 5, we can see that the only considerable error in the solution comes not from the stochasticity, but instead from the angular discretization. We'll explore this further in the next section. It is also clear from Figure 5

16

Table 1: FoM for Timestep Study (64 Angular Bins)

| Method | Particles | $\Delta t = 10^{-12}$ | $\Delta t = 10^{-11}$ | $\Delta t = 10^{-10}$ |
|--------|-----------|------------------------|------------------------|------------------------|
| SMC | 500 | 1 | 1 | 1 |
| RMC | 500 | 331.8 | 68.2 | 50.3 |
| SMC | 5000 | 1.57 | 0.562 | 0.463 |
| RMC | 5000 | 92.2 | 16.8 | 15.5 |
| SMC | 50000 | 0.350 | 0.126 | 0.184 |
| RMC | 50000 | 11.1 | 2.02 | 3.39 |

that using 500 particles will suffice with RMC to eliminate the random error. Hence we can see the degradation of the FoM as the number of particles are increased.
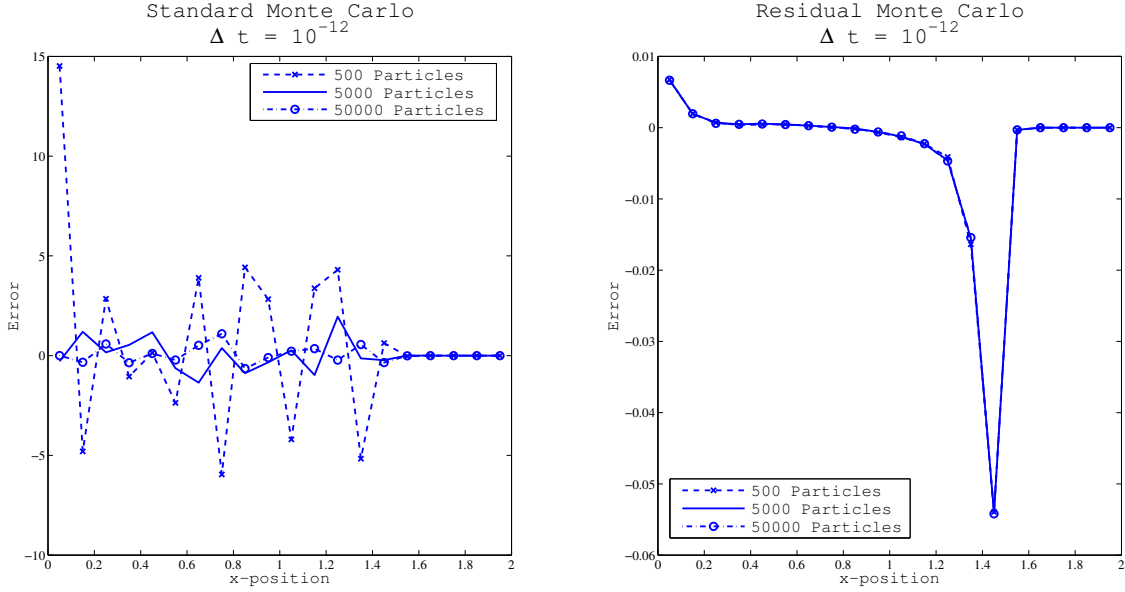


Figure 5: Comparison of SMC and RMC at time-steps of $\Delta t = 10^{-12}$ s. Note the different $y$-axis scales.

### 5.1.2. Sensitivity to Number of Angular Bins

In this section we solve the Marshak wave problem using 16, 64 and 128 angular bins. We fix the number of spatial cells equal to 20 and use
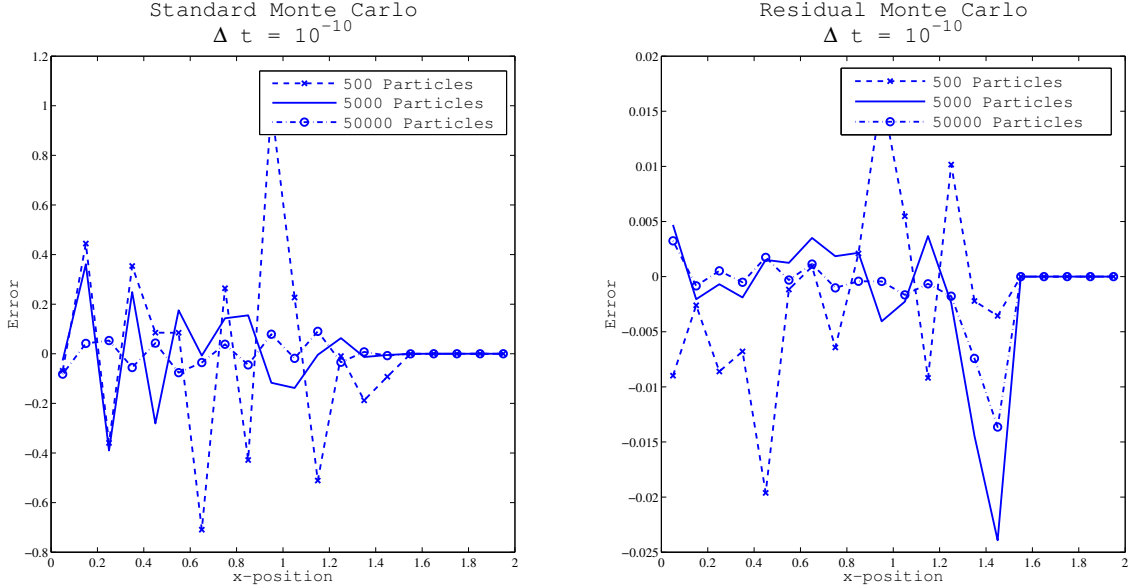
Figure 6: Comparison of SMC and RMC at time-steps of $\Delta t = 10^{-10}$ s. Note the different $y$-axis scales.

timesteps of $10^{-11}$ seconds. The reference solution is computed using a high-accuracy step-characteristics solution using 20 spatial cells ad timesteps of $10^{-11}$ seconds. Again, we normalize such that the FoM for SMC using 500 particles is 1. The FoMs are displayed in Table 2. The first number is a FoM with respect to SMC using the comparable number of angular bins. The second number in parenthesis is a FoM with respect to SMC using 16 angular bins and 500 particles.

As one can see from the table, the FoM increases for RMC as the number of angular bins is increased. The reason for this should be clear – by approximating the angular intensity over a finite number of bins, some angular discretization error is incurred. As the number of angular bins is increased, this discretization error becomes smaller, allowing the RMC solution to approach the benchmark solution. The important thing to note is that when one compares the solution using 16 angular bins with both SMC and RMC, the RMC solution is far less noisy. The FoM is only 6.93 because the dominant error is due to the angular discretization. This can be seen in Figures 7 and 8.

Table 2: FoM for Angular Bin Study

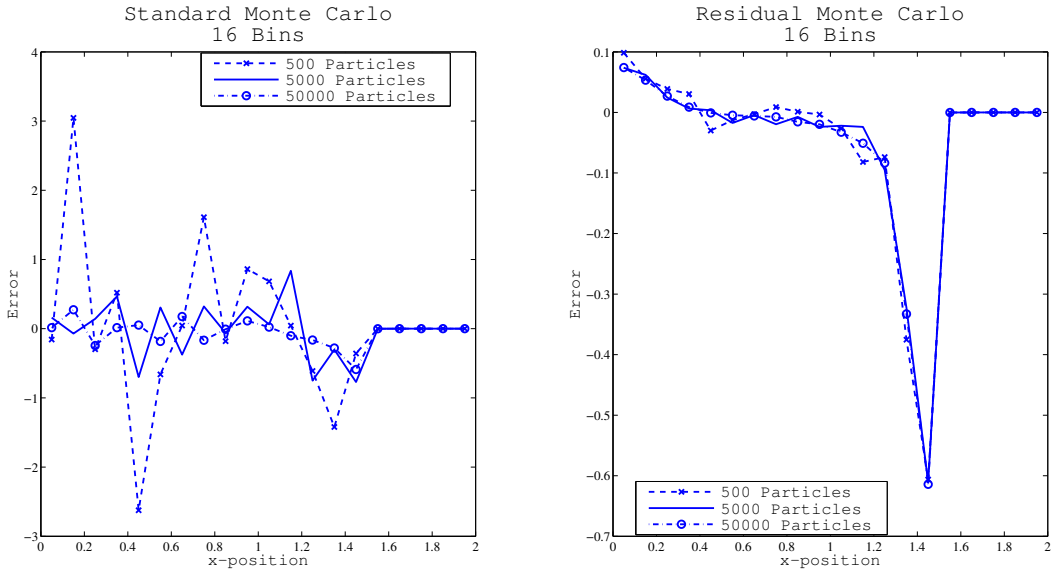| Method | Particles | 16 Bins | | 64 Bins | | 128 Bins | |
|--------|-----------|---------|-----|---------|---------|---------|---------|
| SMC | 500 | 1 | (1) | 1 | (9.012) | 1 | (3.826) |
| RMC | 500 | 6.93 | (6.93) | 68.2 | (614.6) | 272.9 | (1044.1) |
| SMC | 5000 | 0.384 | (0.384) | 0.562 | (5.065) | 0.777 | (2.973) |
| RMC | 5000 | 1.075 | (1.075) | 16.8 | (151.4) | 109.3 | (418.2) |
| SMC | 50000 | 0.0846 | (0.0846) | 0.126 | (1.136) | 0.307 | (1.175) |
| RMC | 50000 | 0.112 | (0.122) | 2.02 | (18.205) | 15.1 | (57.8) |



Figure 7: Using 16 angular bins there is a considerable amount of angular discretization error. This can be recognized by the error at the radiation front at $x = 1.4$ cm. Note the different $y$-axis scales.

These figures also help to demonstrate that the RMC is already "converged in terms of particles" by the time 500 particles are used. It is clear that the stochastic (Monte Carlo) error is smaller than the discretzation error. This is not the case for SMC – as the number of particles per timestep is increased, the error continues to decrease. We can see that RMC with 500 particles contains less error than SMC using 50000 particles. In this sense,
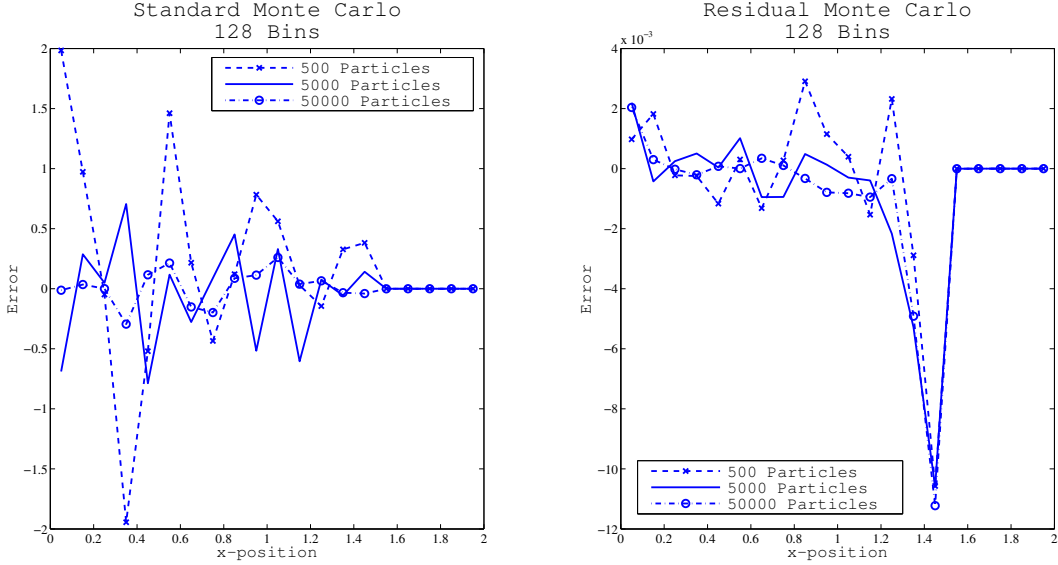
19

Figure 8: Using 128 angular bins we encounter much smaller angular discretization error. This error is still visible at the radiation front, however it is much smaller than when 16 angles are used. Note the different $y$-axis scales.

the FoM is misleading. RMC with 500 particles should really be directly compared to SMC with 50000 particles. This results in an "effective FoM" of nearly 900.

### 5.1.3. Sensitivity to Spatial Mesh Width

In this section we solve the Marshak wave problem using 20 and 100 spatial cells. We fix the number of angular bins equal to 64 and use timesteps of $10^{-11}$ seconds. Again, recall that the reference solutions are computed using a high-accuracy step-characteristics simulation using either 20 or 100 angular bins and timesteps of $10^{-11}$ seconds. As before, we normalize such that the FoM for SMC using 500 particles is 1. The FoMs are displayed in Table 3.

In Figures 9 and 10 we plot the errors for SMC and RMC for two different meshes. On both meshes, SMC is noisier than RMC. When $\Delta x = 0.02$, in Figure 10, we see that using RMC with 50000 particles produces noticeably less noisy results than with 500 particles, but the error is still completely dominated by the angular discretization error. As was seen in Sections 5.1.2

20

Table 3: FoM for Spatial Mesh Study

| Method | Particles | $N_x = 20$ | $N_x = 100$ |
|--------|-----------|-----------|-------------|
| SMC | 500 | 1 | 1 |
| RMC | 500 | 68.2 | 35.5 |
| SMC | 5000 | 0.562 | 1.267 |
| RMC | 5000 | 16.8 | 16.6 |
| SMC | 50000 | 0.126 | 0.188 |
| RMC | 50000 | 2.02 | 2.54 |

and 5.1.3, the RMC algorithm produces much higher quality results at a fraction of the number of particles per timestep required by SMC.
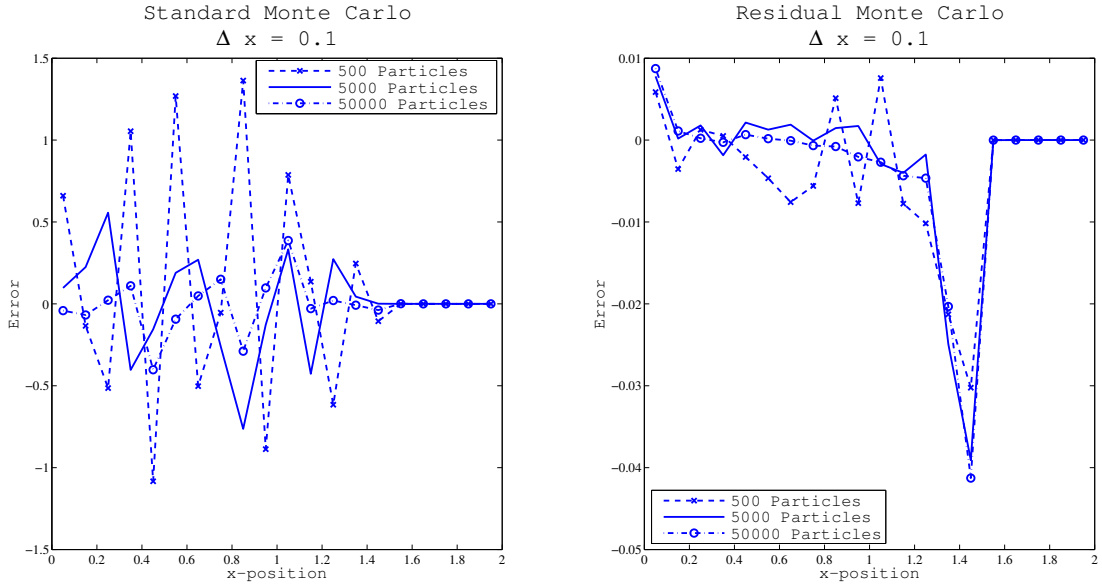


Figure 9: Comparison of SMC and RMC at $\Delta x = 0.1$. Note the different $y$-axis scales.

*5.2. 1-D Gray Two-Material Problem*

This problem represents a multi-material domain in which there exists a sharp material interface. Half way through the domain there is a transition from an optically thin material to an optically thick material. We consider a
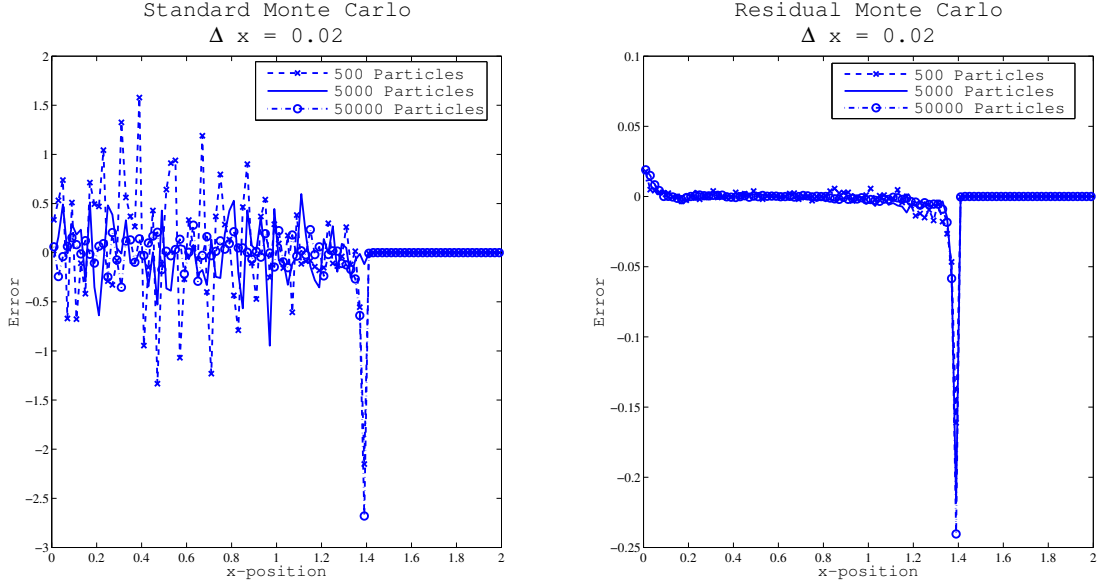
Figure 10: Comparison of SMC and RMC at $\Delta x = 0.02$. Note the different $y$-axis scales.

1.0 cm domain which is initially in equilibrium at 50 eV. At $t = 0$ we apply a 500 eV isotropic incident intensity at the left edge of the domain. The rest of the material properties are summarized in Table 4. We ran each simulation to a final time $t = 5\ sh$ ($1\ sh = 10^{-8}s$) using a maximum time-step of $\Delta t = 10^{-11}s$.

Table 4: Material Properties for 1-D 2 Material Problem

|  | Material 1 | Material 2 |
|---|---|---|
| $x$ - range | < 0.5 cm | > 0.5 cm |
| $\sigma$ (cm$^{-1}$) | 0.2 | 2000 |
| $\rho$ (g/cm$^3$) | 0.01 | 10.0 |
| $c_v$ (erg/eV-g) | $10^{12}$ | $10^{12}$ |

We will vary the number of angular bins, using either 64 or 128, and apply spatial meshes with 40 or 100 cells. While a more exhaustive study was performed for the Marshak wave problem, we only seek to demonstrate here that the same general trends are observed. The FoM for each of these

22

problems are presented in Tables 5 and 6.

Table 5: FoM for Two-Material Problem using 40 Spatial Cells

| Method | Particles | 64 Bins | 128 Bins |
|--------|-----------|---------|----------|
| SMC | 500 | 1 | 1 |
| RMC | 500 | 4917.8 | 6468.5 |
| SMC | 5000 | 1.734 | 0.498 |
| RMC | 5000 | 2450.4 | 4274.5 |
| SMC | 50000 | 0.462 | 0.313 |
| RMC | 50000 | 435.0 | 969.3 |

Table 6: FoM for Two-Material Problem using 100 Spatial Cells

| Method | Particles | 64 Bins | 128 Bins |
|--------|-----------|---------|----------|
| SMC | 500 | 1 | 1 |
| RMC | 500 | 4583.2 | 12307.7 |
| SMC | 5000 | 1.189 | 3.193 |
| RMC | 5000 | 3031.6 | 9867.6 |
| SMC | 50000 | 0.340 | 1.262 |
| RMC | 50000 | 680.9 | 3106.6 |

In each of these tables we can see that RMC is a significant improvement over SMC. The FoMs for the Two-Material problem are even higher than that for the Marshak wave problem. This can be explained because there is a strong emission source that needs to be simulated even beyond the radiation front. SMC requires particles to be distributed everywhere throughout the domain, and the source in every cell is considerably stronger than that of the Marshak wave. We see the FoM increases for RMC as we use 100 spatial cells and 128 angular bins. When 100 spatial cells and 128 angular bins are used, the SMC solution exhibits $> 10\%$ errors near the material interface due to undersampling. These errors can be seen in Figures 11 through 14.

Figure 14 plainly demonstrates how bad the undersampling error can be for SMC when 500 particles are requested per timestep. These errors are most
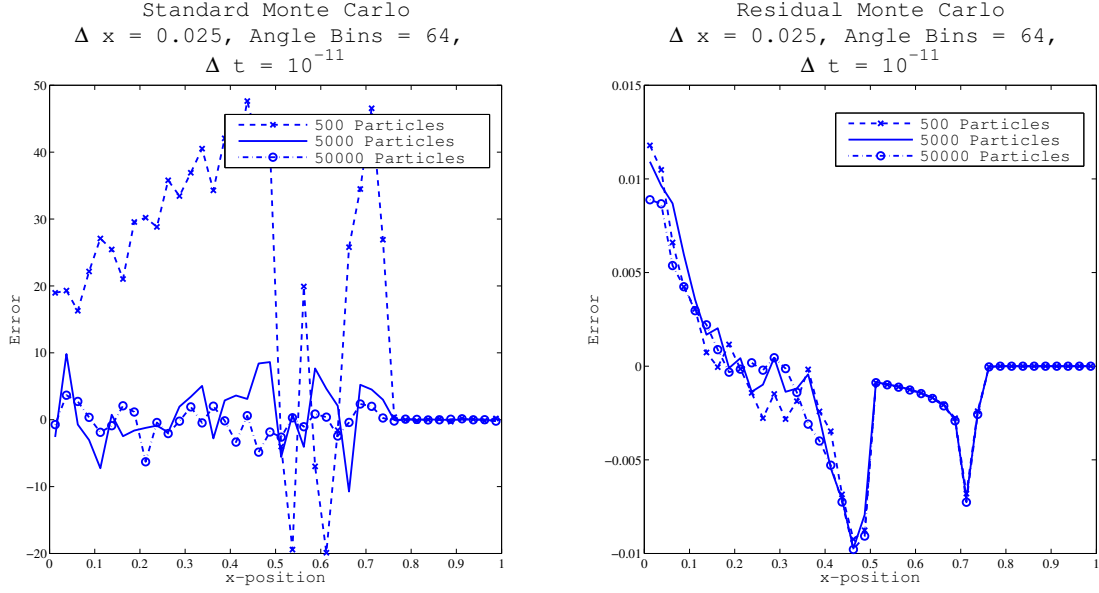
Figure 11: Comparison of SMC and RMC at $\Delta x = 0.025$ with 64 angular bins. Note the different $y$-axis scales.

pronounced in the thin region where particles with large weights are free to stream across many cells. The RMC solution contains very little stochastic error, even when very few particles are used. Again, the only major errors in the RMC come from the angular discretization. For the Two Material problem, RMC can be thousands of times more efficient than SMC.

## 6. Conclusion

Hybrid moment-based acceleration algorithms which rely on a Monte Carlo transport sweep require the high-order solver to return globally accurate solutions. Standard Monte Carlo may become too expensive if we attempt to achieve a high level of accuracy. In this paper, we have presented a residual Monte Carlo algorithm to replace the standard Monte Carlo simulation. The residual Monte Carlo algorithm requires a careful implementation to recover an analytic solution, but this extra work is well worth it. We have demonstrated that we can achieve a high-level of accuracy with the residual Monte Carlo method using hundreds or thousands times fewer particles than would be required with standard Monte Carlo. This is because the residual
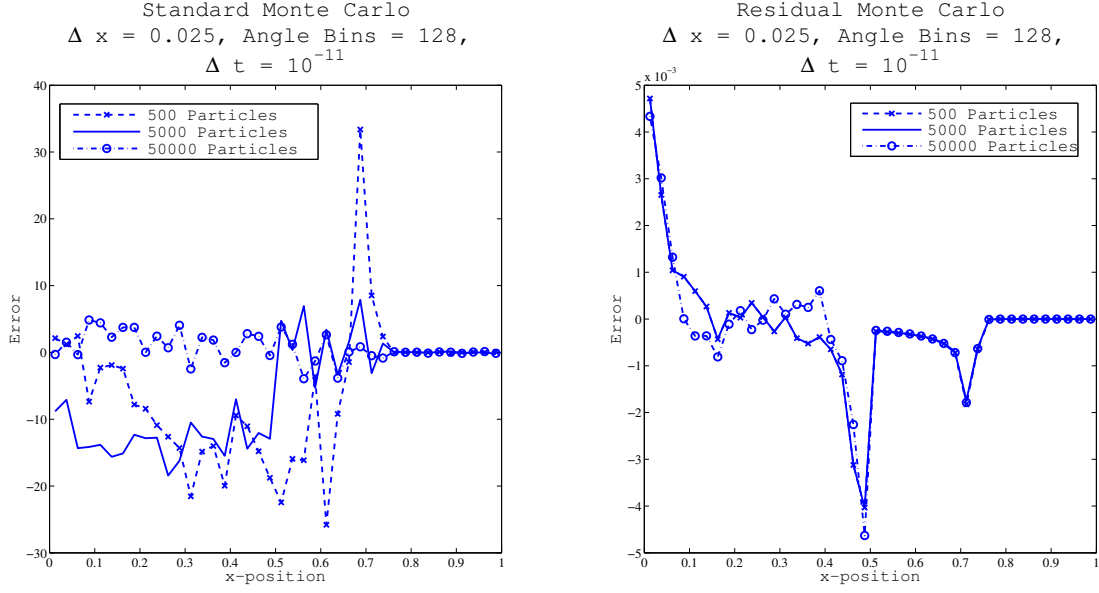
24

Figure 12: Comparison of SMC and RMC at $\Delta x = 0.025$ with 128 angular bins. Note the different $y$-axis scales.

Monte Carlo algorithm allows for a more efficient use of particles by concentrating them in regions of the domain where the solution is rapidly changing. Additionally, with the residual Monte Carlo algorithm, the solution accumulates no error within a cell during a time-step when the solution in that cell is not changing. We demonstrated a clear advantage of the RMC-based HO-LO method with computational results for two 0-D test problems and two challenging 1-D test problems.

Moving forward, the next goal will be to adapt this method to use the time-continuous Monte Carlo method described in [11]. This allows for a more accurate treatment of the time variable. Following the extension of RMC to the time-continuous form, we will work to place RMC in the multi-frequency setting. We expect a straightforward extension to multifrequency problems, with the main concern being the potentially excessive memory consumption required to store the angular intensity at each angle, frequency and point in space at multiple points in time. Finally, we will work to place the RMC method in a multidimensional setting. At this point in time, the only major concern moving to the multidimensional setting is the increased
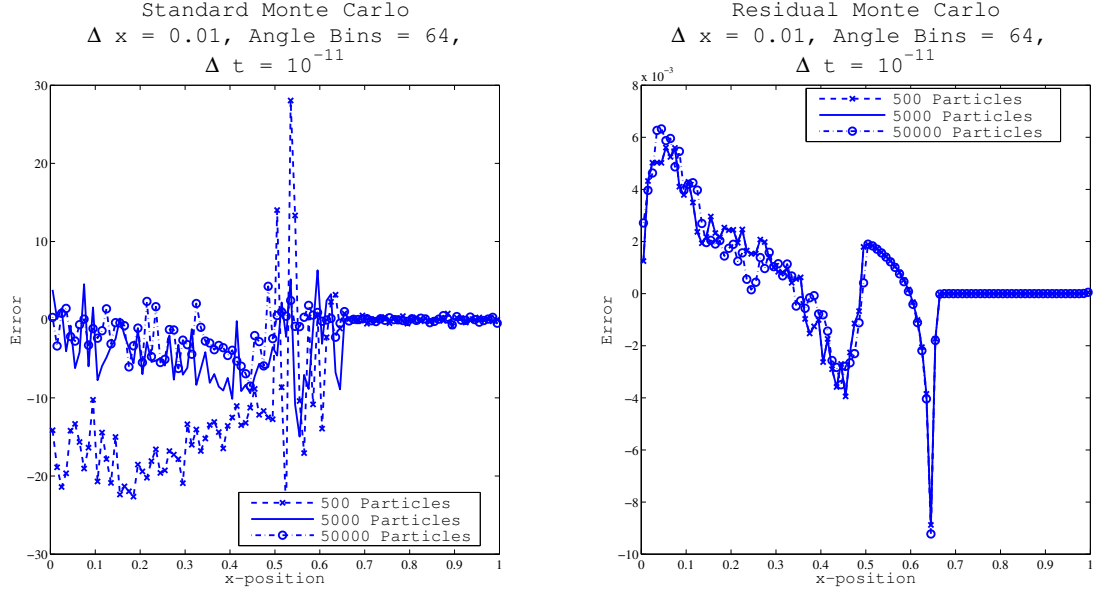
Figure 13: Comparison of SMC and RMC at $\Delta x = 0.01$ with 64 angular bins. Note the different $y$-axis scales.

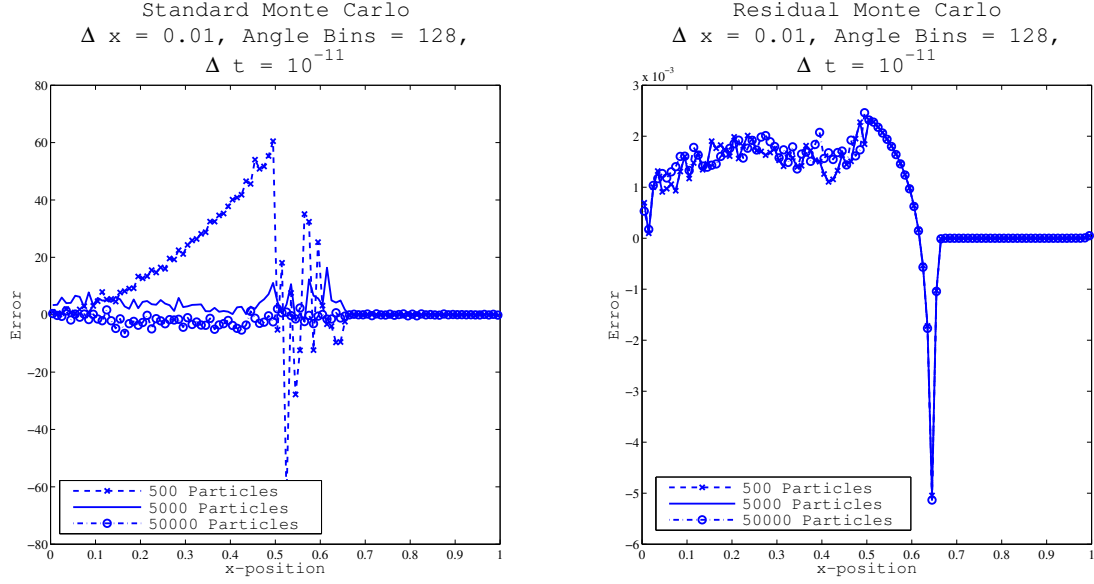memory requirements.

## Acknowledgments

Figure 14: Comparison of SMC and RMC at $\Delta x = 0.01$ with 128 angular bins. Note the different $y$-axis scales.

# References

[1] H. Park, J. D. Densmore, A. B. Wollaber, D. A. Knoll, and R. M. Rauenzahn, *Monte Carlo Solution Methods in a Moment-Based Scale-Bridging Algorithm for Thermal Radiative Transfer Problems: Comparison with Fleck and Cummings*, International Conference on Mathematics and Computational Methods Applied to Nuclear Science & Engineering, Sun Valley, ID, May 5 - 9, 2013.

[2] H. Park, D. A. Knoll, R. M. Rauenzahn, C. K. Newman, J. D. Densmore, and A. B. Wollaber, *An Efficient and Time Accurate Moment-Based Scale-Bridging Algorithm for Thermal Radiative Transfer Problems*, SIAM J. Sci. Comp., vol 35-5, pp 18 - 41, 2013.

[3] H. Park , D. A. Knoll , R. M. Rauenzahn , A. B. Wollaber and J. D. Densmore, *A Consistent, Moment-Based, Multiscale Solution Approach for Thermal Radiative Transfer Problems*, Transport Theory and Statistical Physics, 41:3-4, 284-303, 2012.

[4] Jeffrey Willert, *Hybrid Deterministic/Monte Carlo Methods for Solving the Neutron Transport Equation and k-Eigenvalue Problem*, PhD Thesis, North Carolina State University, Raleigh, North Carolina, 2013.

[5] Jeffrey Willert, C.T. Kelley, D.A. Knoll, and H. Park, *Hybrid Deterministic/Monte Carlo Neutronics*, SIAM J. Sci. Comput., 35(5), 62−83, 2013.

[6] Jeffrey Willert, C.T. Kelley, D.A. Knoll, and H.K. Park, *A Hybrid Approach to the Neutron Transport k-Eigenvalue Problem using NDA-based Algorithms*, International Conference on Mathematics and Computational Methods Applied to Nuclear Science & Engineering, Sun Valley, ID, May 5 - 9, 2013.

[7] D.A. Knoll, Kord Smith, and H. Park. *Application of the Jacobian-Free Newton-Krylov method to nonlinear acceleration of transport source iteration in slab geometry*, Nuclear Science and Engineering, 167(2):122-132, February 2011.

[8] Eugene D. Brooks III, Abraham Szoke, and Jayson D.L. Peterson, *Piecewise linear discretization of Symbolic Implicit Monte Carlo radiation transport in the difference formulation*, Journal of Computational Physics, 220, pp 471-497, 2006.
−

[9] Eugene D. Brooks III, Michael Scott McKinley, Frank Daffin, and Abraham Szoke, *Symbolic implicit Monte Carlo radiation transport in the difference formulation: a piecewise constant discretization*, Journal of Computational Physics, 205, pp 737-754, 2005.

[10] Jacob R. Peterson, Jim E. Morel, and Jean C. Ragusa, *Exponentially-Convergent Monte Carlo for the 1-D Transport Equation*, International Conference on Mathematics and Computational Methods Applied to Nuclear Science & Engineering, Sun Valley, ID, May 5- 9, 2013.

[11] J. Fleck and J. Cummings, *Implicit Monte Carlo Scheme for Calculating Time and Frequency Dependent Non-Linear Radiation Transport*, Journal of Computational Physics, 8:313-342, 1971.

[12] C.T. Kelley, *Iterative Methods for Linear and Nonlinear Equations*, Society of Industrial and Applied Mathematics, Philadelphia, 1995.

[13] C.T. Kelley, *Solving Nonlinear Equations with Newton's Method*, Society of Industrial and Applied Mathematics, Philadelphia, 2003.

**Appendix**

In this section we provide a more rigorous treatment of the derivation in Section 4.2. We compute particle weights by integrating the source function (right-hand-side) of the transport equation over spatial cells and angular bins. Recall from before that we can break the source term down into two components,

$$V = \sigma^{n+1} ac(T^{n+1})^4 - \frac{I^+ - I^n}{c\Delta t} - \sigma^{n+1} I^+ \tag{41}$$

$$B = -\mu \frac{dI^+}{dx}. \tag{42}$$

Integrating $V$ over a space-angle bin is trivial, and the total weight for particles born for $x \in [x_{i-\frac{1}{2}}, x_{i+\frac{1}{2}}]$, $\mu \in [\mu_{j-\frac{1}{2}}, \mu_{j+\frac{1}{2}}]$ is given by

$$W_{i,j} = \left[ \sigma_i^{n+1} ac(T_i^{n+1})^4 - \frac{I_{i,j}^+ - I^n}{c\Delta t} - \sigma_i^{n+1} I_{i,j}^+ \right] \Delta x_i \Delta \mu_j. \tag{43}$$

Treatment of $B$ requires more care. Since $I_{i,j}$ is constant, $\frac{dI}{dx}$ is zero within a cell and does not exist at cell faces unless $I_{i,j} = I_{i+1,j}$. The angular intensity can be represented by a Heaviside function at a given cell interface,

$$I(x, \mu_j) = I_{i,j} + H(x - x_{i+\frac{1}{2}}) (I_{i+1} - I_i), \tag{44}$$

for $x \in (x_{i-\frac{1}{2}}, x_{i+\frac{3}{2}})$. In the sense of distributions, we have

$$\frac{dI(x, \mu_j)}{dx} = \delta(x - x_{i+\frac{1}{2}}) (I_{i+1} - I_i), \tag{45}$$

Integrating $\mu \frac{dI}{dx}$ provides source terms exclusively at cell faces, and the source term is given by

$$W_{i+\frac{1}{2},j} = \bar{\mu}_j (I_{i+1} - I_i) \Delta \mu_j, \tag{46}$$

where $\bar{\mu}_j$ is the average $\mu$ over the $j^{th}$ angular bin.

---

**Algorithm 1** Predictor-Corrector (PC) Algorithm

**PC Time-Step**

Input old time-step solutions, $I^n$, $E^n$, $\vec{F}^n$, $T^n$, $\sigma^n$, and $\gamma^n$.

Solve Predictor LO System

$$\frac{E^* - E^n}{\Delta t} + \nabla \cdot \vec{F}^* + c\sigma^n E^* = \sigma^n ac(T^*)^4$$

$$\frac{\vec{F}^* - \vec{F}^n}{c\Delta t} + \frac{c}{3}\nabla E^* + \sigma^n \vec{F}^* = \gamma^n cE^*$$

$$\rho c_v \frac{T^* - T^n}{\Delta t} - \left(\sigma^n cE^* - \sigma^n ac(T^*)^4\right) = 0.$$

Update opacity $\sigma^{n+1} = \sigma(T^*)$.

Execute a single HO solve,

$$\frac{I^{n+1} - I^n}{c\Delta t} + \hat{\Omega} \cdot \nabla I^{n+1} + \sigma^{n+1} I^{n+1} = \frac{\sigma^{n+1} ac(T^*)^4}{4\pi}. \qquad (12)$$

Compute high-order moments

$$E^{HO,n+1} = \frac{1}{c} \int_{4\pi} d\hat{\Omega} I^{n+1}$$

$$\vec{F}^{HO,n+1} = \int_{4\pi} d\hat{\Omega} \hat{\Omega} I^{n+1}.$$

Compute new consistency term

$$\frac{\vec{F}^{HO,n+1} - \vec{F}^{HO,n}}{c\Delta t} + \frac{c}{3}\nabla E^{HO,n+1} + \sigma^{n+1} \vec{F}^{HO,n+1} = \gamma^{n+1} cE^{HO,n+1}$$

Solve Corrector Step

$$\frac{E^{n+1} - E^n}{\Delta t} + \nabla \cdot \vec{F}^{n+1} + c\sigma^{n+1} E^{n+1} = \sigma^{n+1} ac(T^{n+1})^4$$

$$\frac{\vec{F}^{n+1} - \vec{F}^n}{c\Delta t} + \frac{c}{3}\nabla E^{n+1} + \sigma^{n+1} \vec{F}^{n+1} = \gamma^{n+1} cE^{n+1}$$

$$\rho c_v \frac{T^{n+1} - T^n}{\Delta t} - \left(\sigma^{n+1} cE^{n+1} - \sigma^{n+1} ac(T^{n+1})^4\right) = 0.$$

---

31